Research Square

Preprints are preliminary reports that have not undergone peer review.
They should not be considered conclusive, used to inform clinical practice,
or referenced by the media as validated information.

Post-Fire Seismic Performance of Lightweight RC Beam-Column Joints: Hysteresis, Energy Dissipation and Ductility

Mohammed M. Abed
Urmia University of Technology
Taghi Mofid
Mofid.t@uut.ac.ir
Urmia University of Technology

Research Article

Keywords:

Posted Date: November 10th, 2026

DOI: https://doi.org/10.21203/rs.3.rs-11397399/v1

License: This work is licensed under a Creative Commons Attribution 4.0 International License.
Read Full License

Additional Declarations: No competing interests reported.

Post-Fire Seismic Performance of Lightweight RC Beam-Column Joints: Hysteresis, Energy Dissipation and Ductility

Mohammed M. Abed[1], Taghi Mofid*[1]

[1] Department of Civil Engineering, Urmia University of Technology, Urmia, Iran

Abstract

Fire exposure can substantially alter the post-fire seismic response of reinforced-concrete (RC) beam–column joints, whose performance strongly influences the integrity of moment-resisting frames. This study uses sequential thermal and mechanical finite-element analyses in Abaqus to examine lightweight aggregate concrete (LWAC) joints exposed to 200, 600, and 800 °C and subsequently subjected to cyclic loading. The response is evaluated in terms of hysteresis, backbone curves, load capacity, stiffness, displacement ductility, and hysteretic energy dissipation. Relative to the ambient-temperature model, the peak load decreases from approximately 117 kN to 101, 74, and 48 kN at 200, 600, and 800 °C, respectively, corresponding to reductions of 14%, 37%, and 59%. Displacement ductility also decreases, with reductions of approximately 6.6%, 9.4%, and 40.8%. The energy-based results indicate an even greater loss: cumulative hysteretic energy decreases by 18.3%, 46.5%, and 75.6% at the same temperatures. These findings suggest that energy dissipation may be more sensitive to thermal damage than displacement ductility. Because direct experimental validation for the specific LWAC joint configuration was unavailable, the model was compared with published experimental results for normal-aggregate concrete joints; the predictions should therefore be interpreted as a numerical assessment of relative trends rather than definitive absolute predictions for LWAC joints.

Keywords: Beam-column joints; lightweight reinforced concrete; hysteresis behavior; load capacity; heat exposure.

1. Introduction

The structural integrity of reinforced concrete (RC) frame buildings under extreme loading scenarios, particularly fire events, is critically dependent on the performance of beam-column joints. Recent seismic and fire-induced disasters have highlighted the vulnerability of these joints, which often serve as the weak link in RC frames, dictating the overall strength, deformation capacity, and ductility of the structure [1-4]. With increasing urban density and the prevalence of high-rise constructions, there is a growing imperative to enhance the resilience of these critical connections. Notably, the exposure of RC joints to elevated temperatures during fire can severely compromise their load-bearing capacity and alter their hysteresis behavior, leading to catastrophic failures [5-7]. The structural role of beam-column joints in RC frames is well established. In this regard, joint performance under seismic and fire loading is governed by complex interactions between material degradation and localized heat-

[1] *Corresponding author, Assistant Professor, E-mail: Mofid.t@uut.ac.ir

[1] Master's graduate., E-mail: Mohmhr1199@gmail.com

induced damage [8]. Lightweight aggregate concrete (LWAC) has emerged as a promising material in fire-critical applications due to its inherent thermal insulation properties and reduced self-weight, which can lower seismic demand and dead load on structures [9-11]. However, the mechanical response of LWAC beam-column joints under combined thermal and cyclic loading conditions remains insufficiently understood. LWAC is distinguished by its lower thermal conductivity and improved fire resistance compared to normal-weight concrete. Its porous microstructure imparts superior insulation, mitigating the temperature rise in the core of structural elements during fire exposure [12-15]. Nevertheless, LWAC is also associated with reduced mechanical strength and altered post-peak behavior, which necessitates a careful balance between thermal performance and structural reliability. The application of finite element (FE) modeling to LWAC joints under fire conditions thus requires specialized constitutive models, heat transfer analyses, and robust numerical strategies for assessing hysteresis and load-bearing capacity.

Exposure to elevated temperatures induces a series of deleterious effects in RC joints, including the loss of concrete strength and stiffness, rebar yield reduction, and changes in bond characteristics [16-19]. The heat transfer process within the joint is governed by conduction, convection, and, to a lesser extent, radiation, with temperature gradients leading to differential expansion, cracking, and ultimately, loss of load-carrying capacity. The integration of temperature-dependent mechanical properties, as well as appropriate boundary and initial conditions, is essential for capturing the coupled thermo-mechanical response. Heat transfer within the joint region is a multi-scale phenomenon, influenced by the interaction of concrete, steel reinforcement, and interfacial transition zones [7]. More specifically, the enhancement of heat transfer and the reduction of entropy generation, as key indicators of thermomechanical efficiency, are governed by boundary conditions (e.g., slip, heat flux), material rheology, and geometric configuration [20]. In the context of RC joints, the heterogeneous microstructure of LWAC and the presence of rebar cages create zones of variable conductivity and anisotropy, necessitating the use of detailed FE formulations that account for such complexities. The post-fire or elevated-temperature performance of RC joints is characterized by reductions in yield strength, ductility, and energy dissipation capacity [21]. The hysteresis behavior, typically evaluated via cyclic loading protocols, reflects the ability of the joint to absorb and dissipate seismic or dynamic loads after thermal exposure. The FE method enables the simulation of these phenomena through the implementation of appropriate constitutive models (e.g., damage mechanics, plasticity, bond-slip laws) and the tracking of localized failure mechanisms. The integration of heat transfer and stress analyses into the FE modeling of RC joints offers a holistic perspective on structural degradation mechanisms. For LWAC joints, this suggests that tailored joint detailing and material selection can mitigate the adverse effects of thermal gradients, preserving load-bearing capacity and hysteretic performance.

Although previous studies have examined fire damage and seismic behavior of RC members separately, the post-fire cyclic response of LWAC beam–column joints remains insufficiently characterized. In particular, quantitative comparisons of hysteresis response, strength and stiffness degradation, displacement ductility, and energy dissipation across multiple exposure temperatures are limited. To address this gap, the present study conducts sequential thermal and mechanical finite-element analyses in Abaqus for joint models exposed to 200, 600, and 800 °C and then subjected to displacement-controlled cyclic loading. The study quantifies changes in peak and yield loads, characteristic displacements, ductility, and hysteretic energy

dissipation, with the aim of clarifying how thermal exposure affects the seismic response of the investigated joint. The contribution of this study is a temperature-dependent numerical comparison of several complementary seismic performance indicators for LWAC beam–column joints. The results are intended to support interpretation of post-fire performance and to identify parameters that may warrant particular attention in assessment or retrofit. Since direct experimental data for the exact LWAC joint configuration were not available, the numerical framework is checked against published tests on normal-aggregate concrete joints; this limitation is considered when interpreting the results.

2. Literature Review

Numerous experimental studies have attempted to understand and evaluate the complex behavior of beam-column joints [22, 23]. However, the current knowledge on the seismic behavior of existing RC structures still needs to fill some validation gaps and experimental evidence is still very limited [24]. The relevant experimental results included hysteresis force-displacement diagrams and envelopes, energy dissipation of various components, and strength decay. The observed damage results show that two different failure modes exist in the cyclic tests, including shear failure of the joint core and concrete spalling, followed by buckling of the external longitudinal reinforcement. Accordingly, the weak confinement of the beam longitudinal reinforcement plays an important role in damage evolution of the beam-column joints. In addition, shear failure of the joint is typical [25]. The ultimate damage pattern in experiments show that most of the cracks are located near stirrups, which is due to the concrete discontinuity caused by the stirrups. In this regard, Izadifar and Haji Shabanian [26] experimented with the post-fire seismic behavior of external joints in RC frames. They reported a series of changes in the failure mode of RC joints exposed to high temperatures. Wu et al. [27] conducted an experimental study on the resistance of concrete beam-column joints to earthquake-induced fire. Naeem et al. [28] investigated the performance of beam-column connections exposed to high temperatures. Abdullah et al. [29] experimentally investigated the effect of lightweight aggregate on the mechanical properties of concrete exposed to fire. According to the results, the density, compressive strength, tensile strength, and elastic modulus of concrete decreased when lightweight aggregate was used. The extent of such decrease in these properties increased with increasing aggregate content. However, adding lightweight aggregate reduced mass loss due to fire at all temperatures. The residual compressive strength of concrete decreased with temperature, while a higher amount of aggregate led to better strength retention. The residual compressive strength at 600 °C was 57.1% and 72.0% when 0% and 30% lightweight aggregate was used, respectively. In addition, the tensile strength decreased significantly with increasing temperature. According to the results, concrete containing lightweight aggregate was more resistant to damage, where increasing aggregate content led to better concrete damage performance. Felicceti et al. [30] investigated the thermal and mechanical properties of high-performance LWAC (HPLWC) exposed to high temperatures. The results showed that HPLWC is somewhat more sensitive to temperature than normal-strength concrete (NSC) or LWAC. It was realized that LWAC protects tensile bars more effectively against heat flow by significantly increasing the load-bearing capacity at any fire duration. According to the results, the thermal performance of specimens with LWAC was better than that of NSC.

Chen et al. [31] performed a numerical simulation of the bond-slip analysis of RC wall-beam-slab joints under cyclic loading. The concrete damaged plasticity (CDP) model and the combined hardening structural model were presented and adopted in Abaqus for concrete and reinforcement, respectively. In general, the analysis results showed that numerical results without bond-slip effect overestimate the overall mechanical behavior, while the numerical results including the bond-slip effect are in good agreement with the experimental results. Pothisiri et al. [32] investigated the modeling bond between steel rebar and concrete at high temperatures. A mechanical model was presented based on the theory of smear crack and thick-wall cylinders in the elastic stage. A relationship between bond strength and crack geometry was presented by considering the change in material properties with temperature. Parametric studies were also conducted to investigate the effect of varying concrete compressive strength, concrete cover, and temperature on the degradation of bond strength. Etemadi and Fallahnezhad [33] investigated the behavior of internal RC beam-column joints under lateral loading through FE modeling. Force-displacement curves were generated for joints with different geometric parameters. The effect of beam geometry on mechanical properties, crack types and patterns, plastic hinge length, and plastic dissipation energy of the joint were investigated. It was revealed that increasing the beam width and height reduced the plastic hinge length. For example, the plastic hinge length decreased by 6.5% with a 67% increase in beam width. Stress analysis of the proposed model showed that beam tensile stresses, column compressive stresses, and shear stresses were respectively responsible for the initiation of flexural cracks in beams, narrow flexural cracks in columns, and diagonally-shaped cracks. Also, changing the beam dimensions had a significant effect on the plastic energy dissipation capacity. For a given amount of lateral force, structures with shorter beam widths had higher values of plastic energy dissipation. Recent experimental and analytical studies have further addressed critical aspects of concrete member performance under extreme conditions, including cyclic degradation of lightweight RC beams under periodic loading [34, 35], thermal crack propagation in concrete structures considering rotational ground motion components [36], and post-earthquake residual behavior of RC beams [37], all of which reinforce the necessity of coupled thermo-mechanical assessments for evaluating the seismic resilience of RC components after thermal or seismic damage.

3. Numerical Analysis Methodology

3.1. Joint Geometry and Reinforcement Details

Figure 1 shows the schematic of the RC beam-column joint modeled in this study along with the dimensions and reinforcement details. Also, Table 1 reports the mechanical properties of rebars used in the joint at ambient temperature. Given that the seismic response of the RC joint after fire (fire load in this study refers to temperatures of 200, 600 and 800 °C) is strongly affected by the temperature distribution during fire, the seismic behavior of the investigated joint after fire was analyzed using sequential thermal and mechanical analyses available in the Abaqus software. The analysis was performed in two sequential stages. First, a transient heat-transfer analysis was used to obtain the temperature field in the joint and its components. The resulting nodal temperatures were then transferred to the mechanical model, where temperature-dependent material properties were used in the subsequent cyclic analysis. Because direct post-fire mechanical data for the exact LWAC joint configuration were

unavailable, the temperature-dependent properties were compiled from published studies, as described in Section 3.3.

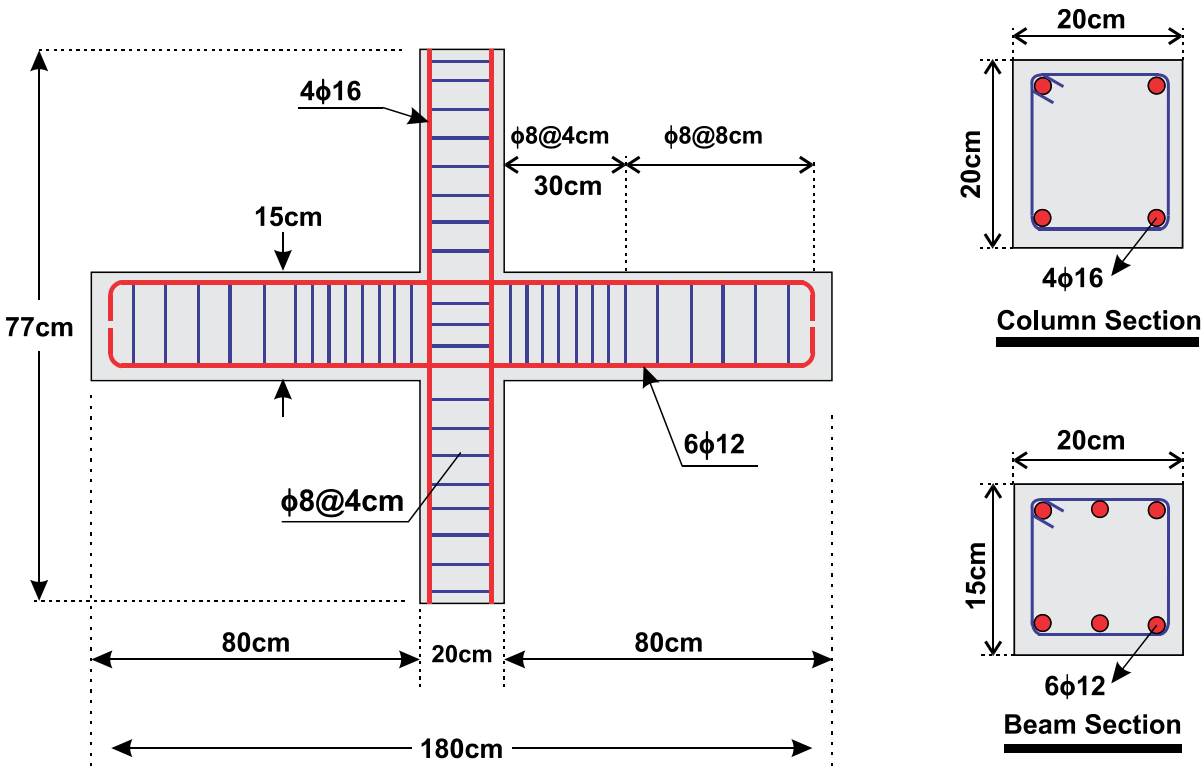


Figure 1. RC beam-column dimensions and reinforcement details

Table 1. Mechanical properties of rebars used in RC beam-column joints

Rebar Type	Elastic modulus (GPa)	Tensile strength (MPa)	Yield strength (MPa)
Φ8	200	620	420
Φ12	200	620	420
Φ16	200	620	420

3.2. Thermal Analysis

The material thermal parameters were primarily specified so as to examine temperature fields in RC joints. The thermal parameters of rebars were specified using the recommendations of Eurocode 4 [38]. In addition, the thermal parameters of LWAC were determined based on the relationships recommended by Eurocode 2 [39]. It is worth noting that the specific weight of LWAC was taken as 1900 kg/m^3. Accordingly, a numerical model for heat transfer analysis was created in Abaqus to capture the temperature distribution of RC joint members after fire exposure. Accordingly, in order to simulate the fire load with higher accuracy, fire curves recommended by Eurocode 4 were employed in this study, as illustrated in Figure 2. Regarding the type of heat transfer, convection and radiation are assumed to transfer heat in the joint models [40-43]. Therefore, in this study, heat transfer was also carried out using this method. The convection coefficient was defined 25 W/m.°C.

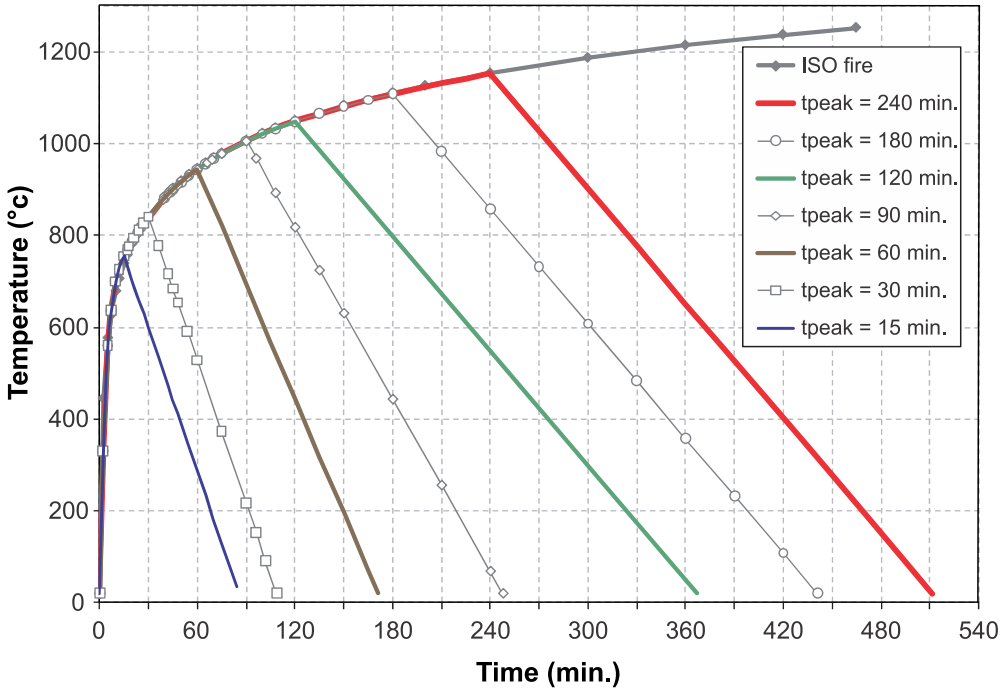


Figure 2. Fire curves in Eurocode 4 [38]

Also, the radiation coefficient of 0.5 and the Stefan-Boltzmann constant of 5.67×10^{-8} W/m^2.K^4 were considered [44]. Moreover, the internal heat transfer in structural components was assumed as conduction. For concrete and steel elements, concrete materials were simulated using 8-node hexagonal linear heat transfer elements DC3D8 and rebars were simulated using 2-node heat transfer elements DC1D2. The thermal resistance between rebars and concrete is very low and does not have a significant effect on the temperature fields, so this was ignored and a value of zero was entered in the software.

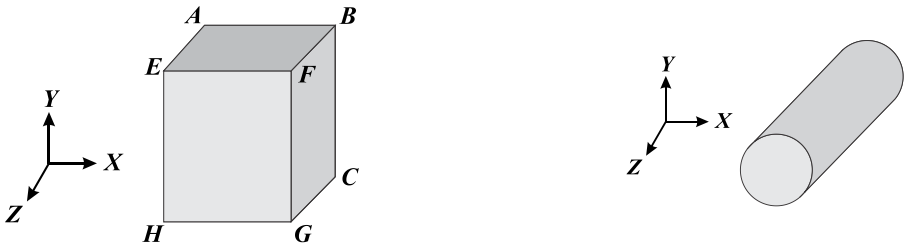
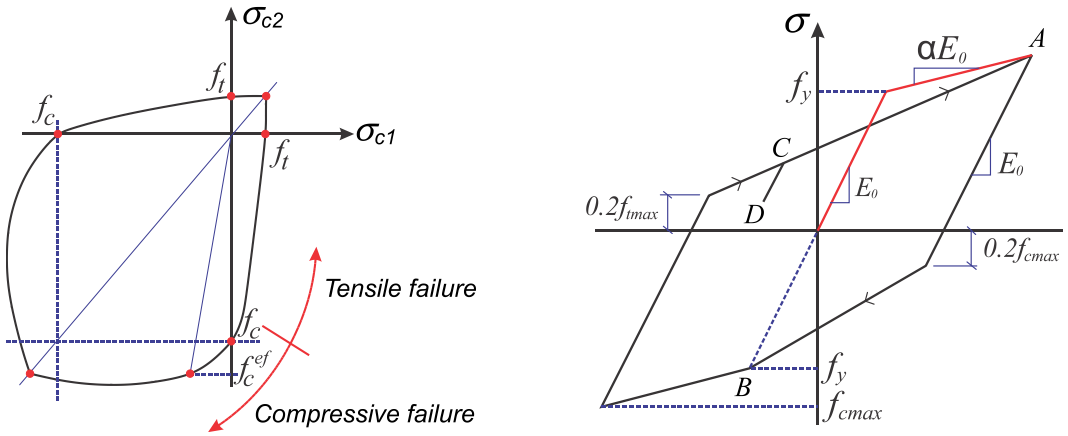


Figure 3. Definition of (a) DC3D8 and (b) DC1D2 elements used for concrete and rebar in ABAQUS

The target exposure temperatures were 200, 600, and 800 °C, corresponding approximately to 15, 60, and 120 minutes on the adopted standard fire curve (ISO 834/Eurocode 4) [38]. All external member surfaces were treated as fire-exposed except symmetry planes and support regions. The cooling phase was not modeled; consequently, the subsequent mechanical analysis represents the response associated with the prescribed heated state rather than a complete heating–cooling fire history.

3.3. Mechanical Properties and Constitutive Models

It is acknowledged that the mechanical properties of both rebar and concrete decrease during fire, like strength and Young's modulus [45]. Thereby, the seismic performance of the joint components as well as the joint itself in general also decrease. To simulate these effects, a suitable thermos-mechanical damage model, types of element, interaction relationships between the two materials of concrete and steel, and mesh size must first be determined.



(a) (b)

Figure 4. Definition of (a) concrete and (b) steel failure functions in Abaqus

During the simulation of seismic performance after fire, the mechanical property damage induced by temperature must be accounted for. Therefore, in order to define rebar thermos-mechanical damage model, damage model to be applied in the replication was determined. In this regard, LWAC has better thermal resistance than NSC, so that the trend of mechanical properties of LWAC when exposed to fire is clearly different from NSC. The responsible factor in applying this difference in the Abaqus software is the thermomechanical damage model of concrete. In order to determine the mechanical damage model of concrete after fire, the mechanical properties of LWAC types after high temperatures were taken from articles and sources in the technical literature [46-72] and the results were reported as the average of these data in Table 2. Finally, these numbers were entered in the modeling of the behavior of lightweight concrete in the software.

Table 2. Definition of mechanical properties of LWAC in Abaqus

Temperature/Property	Compressive strength (MPa)	Tensile strength (MPa)	Elastic modulus (GPa)	Peak strain (%)	Ultimate strain (%)
20 °C	30.00	2.70	22.00	0.0025	0.0045
200 °C	27.60	2.24	17.80	0.0035	0.0063
600 °C	15.00	1.13	7.70	0.0065	0.0122
800 °C	5.70	0.51	3.96	0.0088	0.0157

The constitutive relations for RC were selected based on GB50010 [73], as shown in Eq. 1.

$$\begin{cases} y = \dfrac{nx}{n-1+x^n} & x \le 1 \\ y = \dfrac{x}{\alpha(x-1)^2 x} & x \ge 1 \end{cases}$$
$$\begin{cases} x = \varepsilon / \varepsilon_{c,r} \\ y = \sigma / f_{c,r} \end{cases} \quad (1)$$
$$n = \frac{E_c \varepsilon_{c,T}}{E_c \varepsilon_{c,T} - f_{c,T}}$$

in which $f_{c,r}$ denotes concrete peak stress (MPa), and $\varepsilon_{c,r}$ represents the conforming peak strain. According to Eq. 1, the parameters n and α are described by the peak stress and strain, as well as the Young's modulus and concrete deformation, as quantified in Table 3.

Table 3. Parameters n and α for LWAC at different temperatures [73]

Temperature (°C)	***n***	***α***
20	1.90	49.31
200	2.17	72.44
600	2.20	1.08
800	1.99	0.68

The degradation of concrete material properties under cyclic loading is to some extent irreparable and the concrete is considered crushed. Therefore, the degradation of elastic modulus in each cycle needs to be accounted for. The damage parameters can be determined from the stress ratio of the descending part of the stress-strain curve of concrete. Therefore, the thermal damage index $d(T)$ according to Eq. 2 was introduced into the model [74].

$$d(T) = 1 - \sqrt{\frac{\sigma}{E_c(T)\varepsilon}} \quad (2)$$

in which $E_c(T)$ shows the initial modulus of elasticity of concrete at temperature T. Also, σ and ε are the stress and strain, respectively, at any point on the characteristic curve at any given temperature T. It should be noted that the damage coefficients $d(T)$ are characterized in the damage plasticity model available in Abaqus. As such, the Concrete Damaged Plasticity (CDP) parameters were defined in the software, as expressed in Table 4. The selection of the (CDP) parameters presented in this Table was based on recommendations from previous numerical studies on concrete subjected to thermal and cyclic loading [31-33], as well as the default values suggested in the Abaqus documentation for concrete materials. The dilation angle was set to 30°, which is consistent with the values commonly used for lightweight aggregate concrete in the literature. The eccentricity was taken as 0.1, following the default recommendation in Abaqus for concrete materials. The ratio of biaxial to uniaxial compressive strength was adopted as 1.16, which is the standard value for concrete based on experimental observations [69]. The K value (the ratio of the second stress invariant on the tensile meridian to that on the compressive meridian) was set to 0.67, as recommended for concrete materials in the Abaqus

manual. The viscosity parameter was set to 0.0005 to improve convergence in the numerical analysis without significantly affecting the accuracy of the results, following the recommendations of previous studies [31-33]. These parameters have been validated in numerous numerical investigations on concrete structures under cyclic loading and elevated temperatures [31-33, 69], and are considered appropriate for the present numerical model.

Table 4. CDP parameters for LWAC

Dilation angle	Eccentricity	f_{b0}/f_{c0}	K	Viscosity parameter
30	0.1	1.16	0.67	0.0005

In order to define rebar thermomechanical damage model, material was replicated via a bilinear hardening model, which considers both the effect of Bauschinger and the rebar cyclic hardening. During reversed cyclic loading, the rebars elastic limit in changing compression and tension decreases significantly. When the yield point is reached, the fracture resistance increases and the strain decreases. When the rebars under reversed cyclic load reach the yield strength, the Bauschinger effect and the cyclic hardening effect are considered. The bilinear hardening model of Abaqus matches the linear elasticity and elasto-plasticity curves of rebars under reversed cyclic load, so this model was selected for modeling and simulating the rebars, as recommended by Shen et al. [75]. The bond-slip behavior between concrete and rebar under elevated temperatures is not predefined in Abaqus and was therefore implemented using nonlinear spring elements. The details of the bond-slip model are presented in Section 4.2.

3.4. Loading, Boundary Conditions, and Mesh Configuration

A constant axial compression ratio of 0.2 was applied at the top of the column, together with a horizontal, displacement-controlled cyclic load following the protocol illustrated in Figure 5. The lower column end was restrained against translation in the X, Y, and Z directions; the upper end was free to translate in X and Z. Beam-end translations and rotations were restrained as specified in the model.

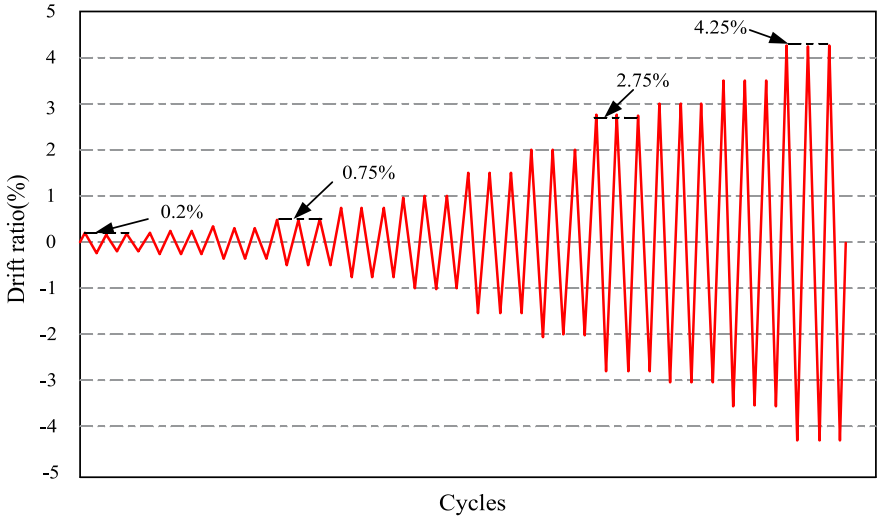


Figure 5. Cyclic load pattern [76]

The loading history comprised three cycles at each increasing displacement amplitude, beginning at 0.25δy and progressing through 0.5δy, 0.75δy, 1.0δy, 1.5δy, 2.0δy, 3.0δy, and 4.0δy and beyond, where δy was obtained from the pushover analysis. The loading rate was 0.5 mm/s. To avoid numerical disturbance, the axial load was gradually removed when the joint's residual capacity fell to approximately 85% of its load capacity. The cyclic protocol was based on ATC-24 [74]. The mesh was kept consistent between the thermal and mechanical models so that the computed nodal temperatures could be transferred to the corresponding mechanical model. The selected mesh and the reference points used to apply loading and boundary conditions are shown in Figure 6. The temperature-dependent LWAC properties in Table 2 were obtained by averaging data from the literature [46-72], selected for similarity in aggregate type, ambient compressive strength, and availability of mechanical properties at elevated temperatures. This averaging introduces material-data uncertainty and is one of the limitations considered when interpreting the numerical results.

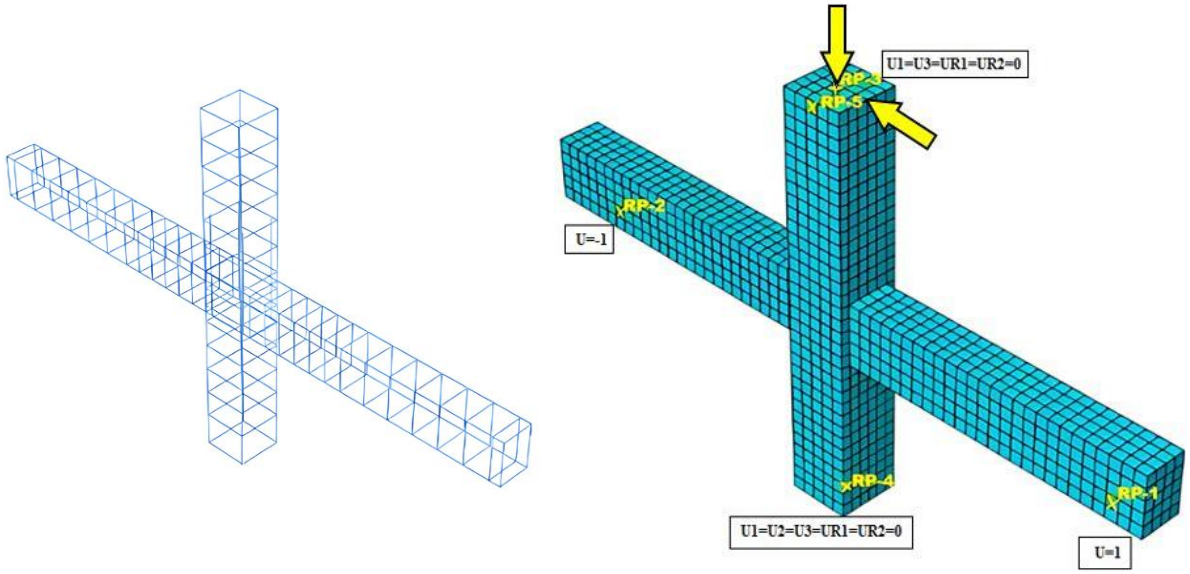


Figure 6. Joint mesh and reference points for load and boundary conditions

4. Modeling and Validation

It is acknowledged that the present numerical model relies on constitutive assumptions derived from averaged experimental data reported in the literature [46-72]. To ensure the reliability of the modeling approach, the adopted thermal and mechanical material properties, as well as the Concrete Damaged Plasticity (CDP) parameters and bond-slip implementation, were carefully selected based on well-established studies on lightweight aggregate concrete (LWAC) and reinforced concrete (RC) beam-column joints. Furthermore, in order to verify the accuracy of the numerical model, a direct validation against available experimental data was performed, as described in Section 4.4. This section provides a comprehensive justification for the modeling assumptions and presents the basis for the reliability of the numerical predictions.

4.1 Material Properties and Constitutive Model Parameters

The temperature-dependent mechanical properties of LWAC, the CDP parameters, and the damage evolution law adopted in this study are detailed in Section 3.3 (Tables 2-4). The reinforcing steel was modeled using a bilinear hardening model, as described in Section 3.3. These parameters were selected based on well-established studies on LWAC and RC beam-column joints [31-33, 69].

4.2 Bond-Slip Modeling

The bond-slip relationship between reinforcing steel and concrete was implemented in Abaqus using nonlinear spring elements, following the model proposed by Pothisiri and Panedpojaman [32]. The bond strength was defined as a function of slip, with the maximum bond stress, slip at peak stress, and ultimate slip calibrated based on experimental data from the literature for lightweight aggregate concrete at elevated temperatures [31-33]. Temperature-dependent reduction factors of 0.85, 0.65, and 0.45 were applied to the bond strength at 200, 600, and 800°C, respectively, consistent with previous studies. The model was verified by comparing the numerical predictions with experimental results, confirming its capability to capture bond deterioration under thermal exposure.

4.3 Mesh Convergence Study

A mesh convergence study was conducted to ensure that the numerical results are independent of mesh discretization. Three different mesh configurations with element sizes of 75 mm, 50 mm (the size adopted in this study), and 35 mm were examined on the reference joint model (BCJ-L20). Reducing the element size from 75 mm to 50 mm resulted in a 4.2% change in the peak load capacity, while further refinement from 50 mm to 35 mm led to only a 1.8% change. The variation in ultimate displacement was less than 3% between the 50 mm and 35 mm meshes. Based on these results, the 50 mm mesh was selected as it provides a good balance between accuracy and computational efficiency. Thus, the selected mesh size ensures mesh-independent predictions of the structural response.

4.4 Validation with Experimental Model

In order to perform a precise comparison between the numerical results and the experimental data reported by Azadi Kenari et al. [77], three FE models were constructed with the specifications summarized in Table 5. These models were made of normal aggregate concrete (NAC) with a compressive strength of 43 MPa and were subjected to temperatures of 25, 300, and 650 °C. The numerical results obtained from the FE analysis were systematically compared with the experimental hysteresis curves reported by Azadi Kenari et al. [77] for the corresponding NAC joint specimens tested at three distinct temperature levels.

Table 5. Specifications of the studied specimens

Specimen	Concrete Type	Concrete Compressive Strength (MPa)	Applied Temperature (°C)
NAC-H25	Normal	43	25
NAC-H300	Normal	43	300
NAC-H650	Normal	43	650

Figure 7 illustrates this comparison by presenting the hysteresis load–displacement curves predicted by the FE model alongside those recorded during the experimental program at temperatures of 25, 300, and 650 °C. The comparison was carried out with particular attention to several key response characteristics, including the overall shape and enclosure of the hysteresis loops, the peak load attained in each cycle, the initial stiffness of the joint, the rate and pattern of strength degradation, and the extent of pinching behavior observed throughout the loading history. The numerical curves reproduce the principal features and temperature-related trends of the experimental hysteresis response, including the overall envelope, peak-load behavior, and progressive stiffness and strength degradation. Some differences remain, particularly in initial stiffness and the degree of pinching during later cycles. These discrepancies may reflect simplifications in the constitutive descriptions, idealized boundary conditions, and differences between the experimental specimens and the numerical representation. The comparison supports the use of the modeling strategy for examining general response trends; however, because the validation specimens contained normal-aggregate concrete, it does not independently establish the absolute accuracy of predictions for LWAC joints. The parametric results are therefore interpreted primarily in terms of relative changes with temperature.

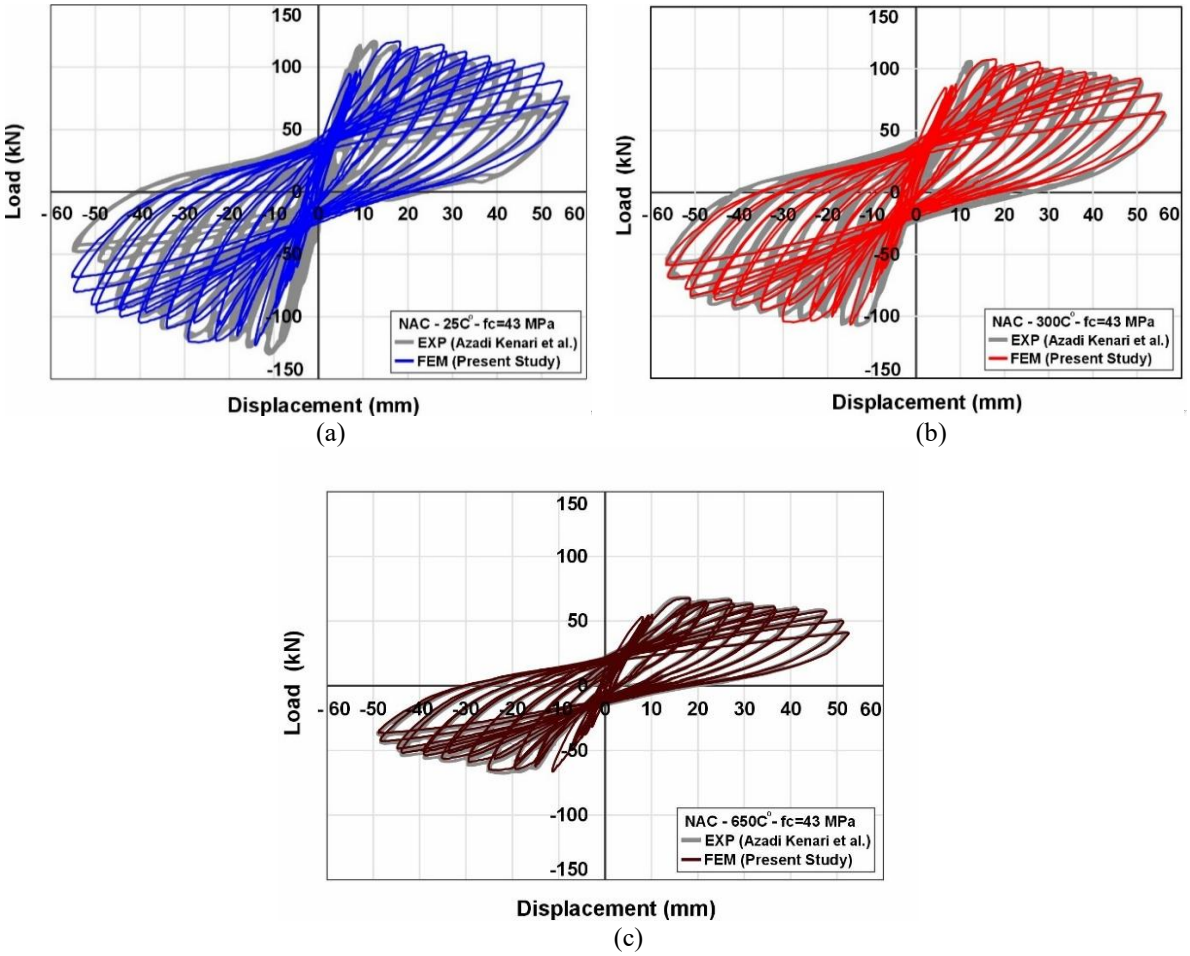


Figure 7. Comparison of hysteresis load-displacement curves between the FE model and the experimental results of Azadi Kenari et al. [77] at temperatures of (a) 25 °C, (b) 300 °C, and (c) 650 °C.

4.5 Limitations and Summary

While the present numerical model provides valuable insights into the seismic performance of LWAC beam–column joints under thermal exposure, certain limitations should be acknowledged. First, although the model was validated against the experimental data of Azadi Kenari et al. [77] for normal-weight concrete, direct experimental validation for LWAC joints specific to the configuration and mixture used in this study was not available. Second, the bond-slip model does not fully capture the localized effects of fire-induced spalling or the complex interaction between reinforcement and concrete at the micro-scale. Third, the cooling phase following fire exposure was not considered in this study, as the focus was on the maximum temperature state. Despite these limitations, the primary objective of this study is to evaluate the relative performance of LWAC joints compared to the ambient-temperature condition, rather than to predict absolute values with high precision. The validation against the experimental data of Azadi Kenari et al. [77] at three temperature levels (25, 300, and 650 °C) provides confidence in the reliability of the numerical framework, as the model successfully captured the key trends of strength degradation, stiffness reduction, and hysteresis behavior. The consistency of the adopted assumptions with the existing body of literature and the observed parametric trends further support the reliability of the numerical results. Future research should focus on conducting dedicated experimental tests on LWAC beam–column joints under combined thermal and cyclic loading to provide direct validation data for numerical models.

5. Parametric Analysis Results

The following results compare the seismic response of the LWAC beam–column joint models at 20, 200, 600, and 800 °C. The mechanical properties assigned to the materials degrade with temperature, while the bond-slip model represents a concurrent reduction in stress transfer between reinforcement and concrete. These effects influence the joint-level response through changes in stiffness, peak resistance, deformation capacity, hysteresis-loop shape, and energy dissipation. The discussion below separates these response measures to avoid repeating the same observations in multiple subsections. The reduction in resistance is consistent with the temperature-dependent properties in Table 2: at 600 °C, the LWAC compressive strength decreases from 30.0 to 15.0 MPa and its elastic modulus from 22.0 to 7.7 GPa. Tensile strength falls even more sharply, from 2.70 MPa at 20 °C to 1.13 MPa at 600 °C and 0.51 MPa at 800 °C. Such losses reduce stiffness and the capacity to resist diagonal tension cracking. In combination with degraded reinforcement–concrete bond, they help explain the lower peak loads and the tendency toward earlier shear failure at elevated temperatures. These mechanisms are interpretations of the numerical response rather than direct observations of physical specimens.

5.1 Hysteresis load-displacement curves

Figure 8 shows the cyclic load–displacement response of the four joint models. At low deformation, the loading and unloading branches largely overlap, indicating a predominantly elastic response, while with continued cycling the loops widen, revealing inelastic deformation and energy dissipation. The ambient-temperature model, BCJ-L20, reaches the highest peak resistance, about 117 kN at roughly 24 mm displacement.

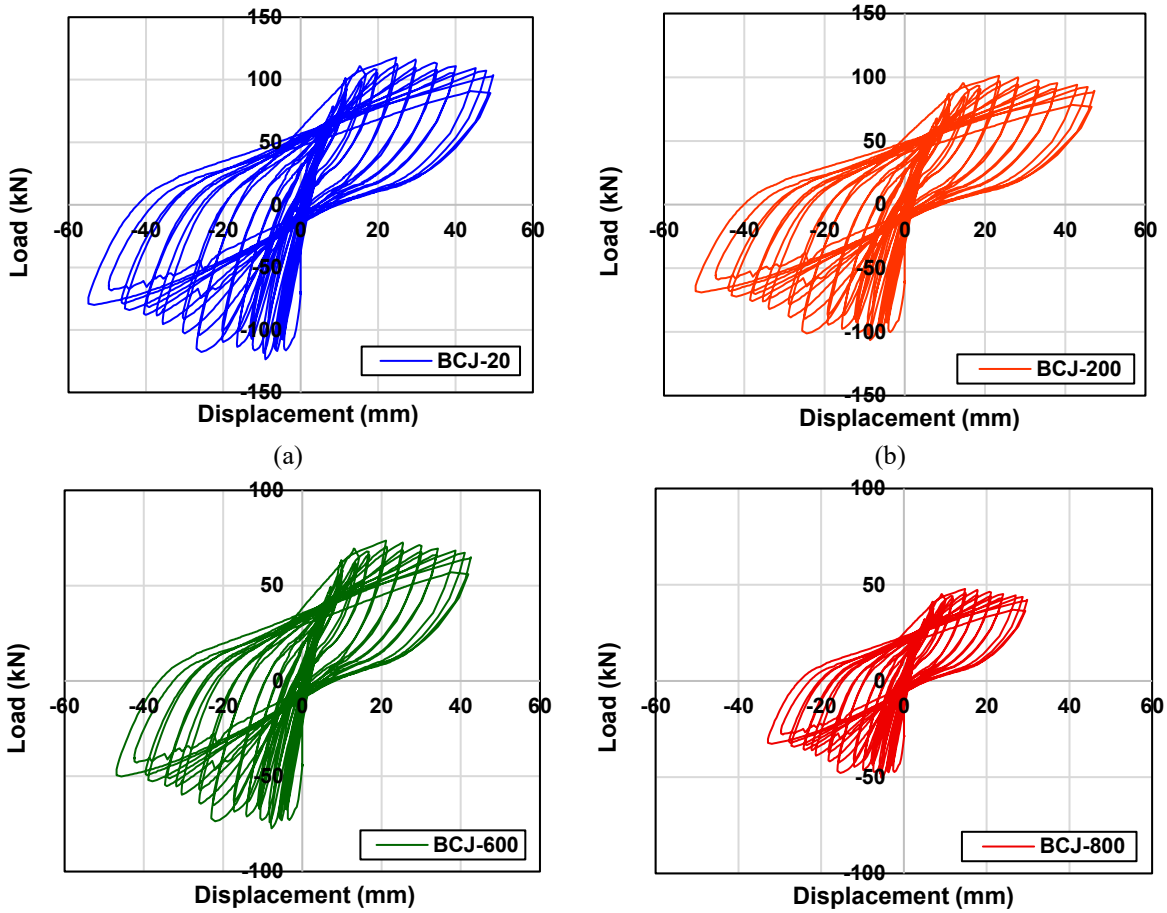


Figure 8. Hysteresis load-displacement curves for LWAC beam-column joint models: (a) BCJ-20, (b) BCJ-200, (c) BCJ-600, and (d) BCJ-800

Peak resistance decreases systematically with exposure temperature. The maximum loads for BCJ-L200, BCJ-L600, and BCJ-L800 are approximately 101, 74, and 48 kN, reached at displacements of 23, 21, and 14 mm, respectively. Relative to BCJ-L20 (approximately 117 kN), these values represent reductions of about 14%, 37%, and 59%. Figure 9 compares the hysteresis responses directly; the progressive narrowing and pinching of the loops at higher temperatures indicate deterioration in cyclic response as well as peak strength. The predicted shift toward earlier shear-dominated failure at elevated temperatures is consistent with trends reported in post-fire and lightweight-concrete studies [46-72]. The comparison is qualitative because aggregate type, mix composition, joint detailing, and loading conditions differ among studies. The reduction in loop area is consistent with the loss of stiffness and reinforcement–concrete bond represented in the model. Lower concrete tensile strength can promote crack opening and reduce aggregate-interlock contribution, while bond deterioration reduces effective stress transfer and increases slip. Together, these mechanisms can produce more pinched loops and smaller enclosed areas.

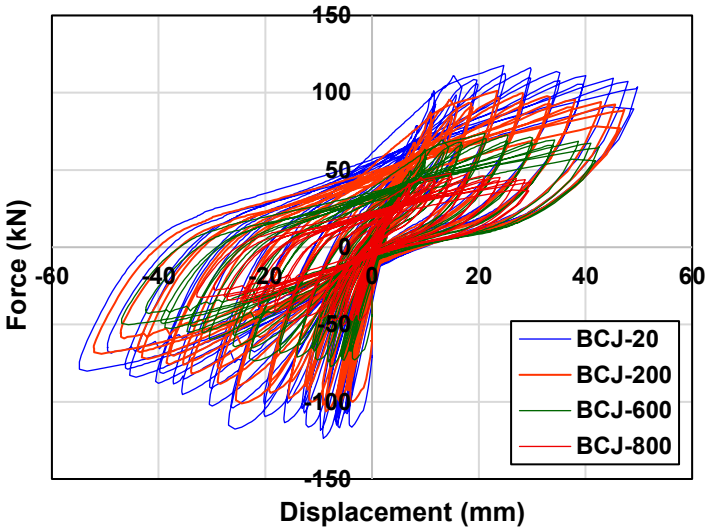


Figure 9. Comparison of hysteresis loops for RC beam-column joints

5.2 Backbone curves

A backbone curve summarizes the peak load reached at each displacement amplitude and provides a clearer view of the envelope of cyclic resistance than the individual hysteresis loops. In this study, the positive and negative peak points from the cyclic response were connected in sequence to construct the backbone curves shown in Figure 10.

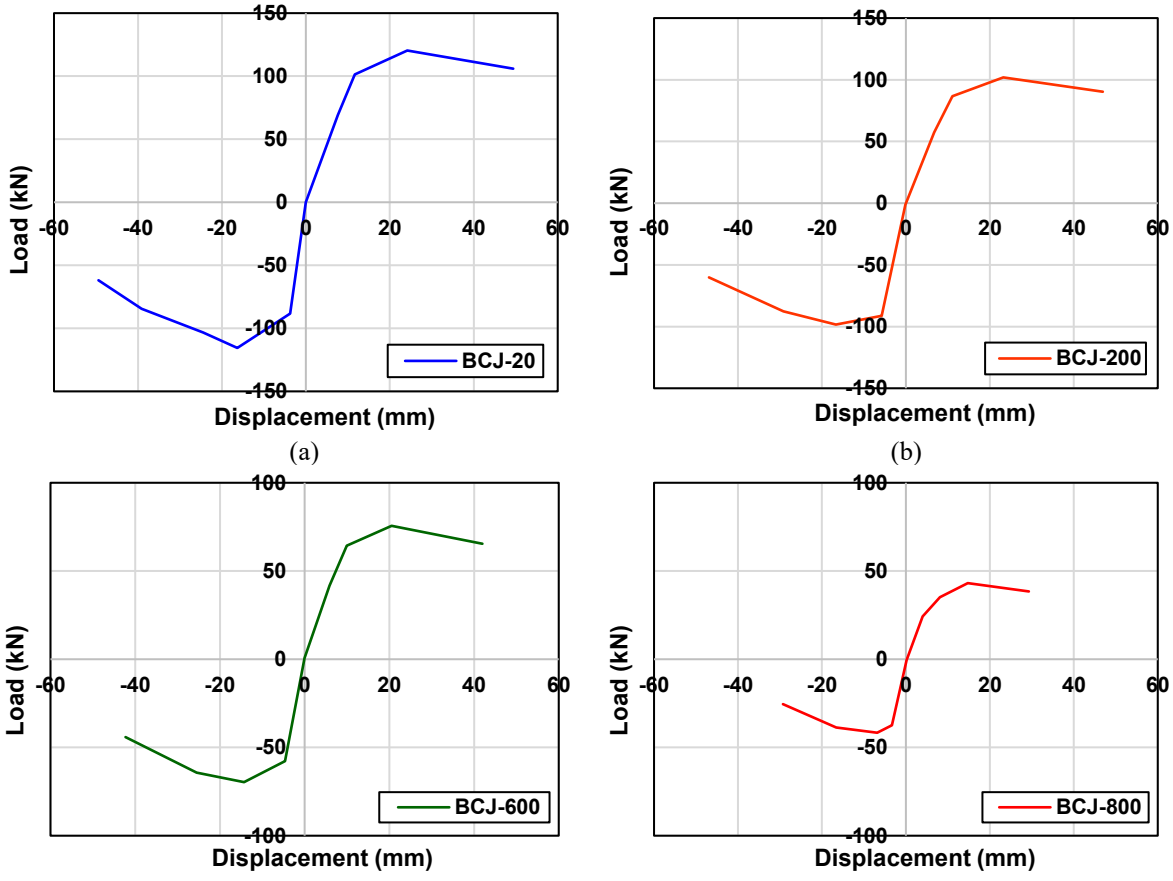


Figure 10. Backbone curves for LWAC beam-column joint models:
(a) BCJ-20, (b) BCJ-200, (c) BCJ-600, and (d) BCJ-800

The displacement at which the model maintained its strength decreased with increasing temperature: the reported values were 11.7 mm for BCJ-L20, 10.6 mm for BCJ-L200, 9.9 mm for BCJ-L600, and 3.9 mm for BCJ-L800. This trend indicates that the high-temperature models reach the onset of strength degradation at smaller displacements, with the most pronounced change occurring at 800 °C. The backbone curves show a temperature-dependent reduction in both resistance and the deformation range over which the joint sustains that resistance. The markedly earlier degradation in BCJ-L800 is consistent with the severe reduction in concrete tensile strength at 800 °C, which can limit diagonal-tension resistance and lead to premature shear failure before the joint develops its full flexural capacity. This interpretation is consistent with the material-property trends in Table 2; it should not be taken as direct experimental identification of the failure mode in the modeled joint.

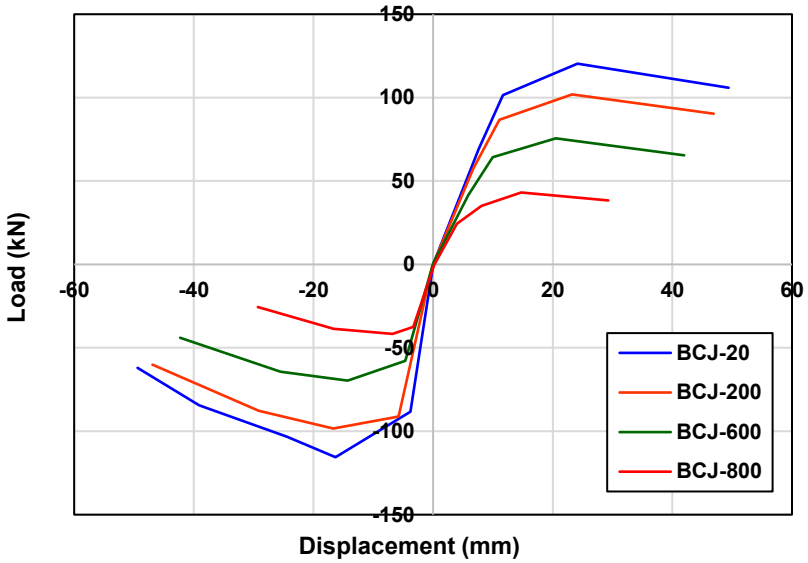


Figure 11. Comparison of backbone curves for RC beam-column joints

5.3 Joint displacement ductility

Three characteristic points were used to evaluate displacement ductility from the backbone curves: the yield point, the peak-load point (P_{max}), and the ultimate point, defined here as the point at which resistance decreases to 85% of Pmax. The yield point and yield displacement (Δ_y) were determined using the equivalent-energy method illustrated in Figure 12, in which the areas on either side of the idealized yield representation are made equal. The ultimate displacement (Δ_u) was taken at the 85%-of-peak criterion, and displacement ductility was calculated as $\mu = \Delta_u/\Delta_y$. Table 6 summarizes the characteristic values. The yield load decreases from 103 kN for BCJ-L20 to 91.4, 69.4, and 39.6 kN for BCJ-L200, BCJ-L600, and BCJ-L800, respectively. The corresponding yield displacements are 12.6, 12.8, 11.6, and 9.94 mm. Ultimate displacement decreases from 49.8 mm for the reference model to 47.2, 41.7, and 23.3 mm as temperature increases. Consequently, the ductility ratio decreases from 3.95 to 3.69, 3.58, and 2.34, equivalent to reductions of approximately 6.6%, 9.4%, and 40.8%. These values show that the most substantial loss of deformation capacity occurs at 800 °C.

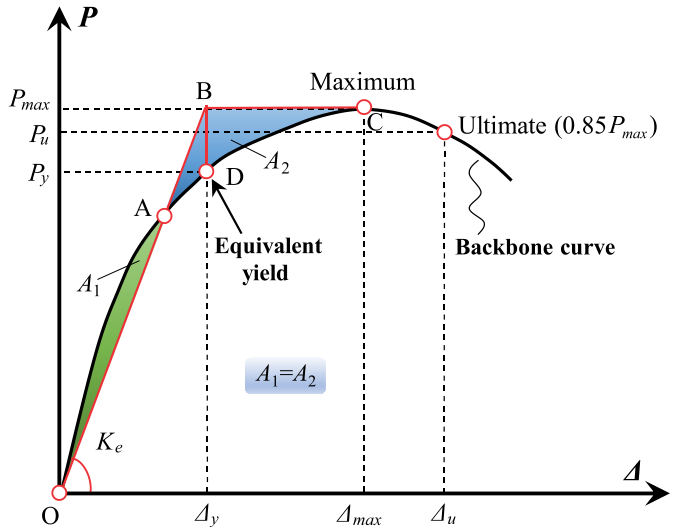


Figure 12. Definition of characteristic points based on the equivalent energy method

The ductility trend reflects the relative changes in ultimate and yield displacement rather than a one-to-one relationship with peak strength. Thermal degradation of the concrete can reduce post-peak deformation capacity through cracking and embrittlement, while the yield displacement is also influenced by reinforcement response and joint stiffness. At 800 °C, the large reductions in concrete strength and stiffness coincide with the sharpest decline in ductility. The proposed mechanisms are consistent with the adopted material models and should be verified by direct tests on LWAC joints.

Table 6. Characteristic points of RC joint models

Model	P_y (kN)	$Δ_y$ (mm)	P_u (kN)	$Δ_u$ (mm)	μ	Ductility Reduction vs. BCJ-20 (%)
BCJ-20	103	12.6	117	49.8	3.95	(Reference)
BCJ-200	91.4	12.8	101	47.2	3.69	6.58
BCJ-600	69.4	11.6	74	41.7	3.58	9.37
BCJ-800	39.6	9.94	48	23.3	2.34	40.76

Hysteretic energy dissipation was evaluated from the area enclosed by the load–displacement loops. Table 7 reports cumulative dissipated energy, the area of the largest loop, and the average loop area for each model. All three measures decrease as exposure temperature increases, indicating that the loss of cyclic energy dissipation is not confined to a single cycle. Cumulative energy decreases from 53,969.50 J for BCJ-L20 to 44,093.08, 28,889.79, and 13,144.85 J for BCJ-L200, BCJ-L600, and BCJ-L800, respectively. These correspond to reductions of 18.30%, 46.47%, and 75.64% relative to the ambient-temperature model. The largest loop area also decreases from 6,350.68 J to 5,188.51, 3,399.51, and 1,546.78 J, while the average loop area falls from 2,075.75 J to 505.57 J between BCJ-L20 and BCJ-L800. A similar trend is observed in the largest loop area, which decreases from 6,350.68 J in BCJ20 to 5,188.51, 3,399.51, and 1,546.78 J in BCJ200, BCJ600, and BCJ800, respectively. The substantial reduction in the largest loop area at higher temperatures indicates that the joints dissipate considerably less energy during the corresponding loading cycles. This trend is also reflected in the average loop area, which decreases from 2,075.75 J for BCJ20 to 505.57 J for BCJ800. The reduction in both the largest and average loop areas confirms that the observed deterioration is not limited

to the cumulative response but is also evident at the individual-cycle level. The reduction in hysteretic energy dissipation can be attributed to temperature-induced deterioration in the mechanical properties of concrete and reinforcing steel, accompanied by degradation of the bond between the reinforcement and the surrounding concrete. These effects can impair stiffness retention, reduce the load-carrying capacity, and alter the shape of the hysteresis loops. Consequently, the joints exhibit a reduced capacity to dissipate energy through repeated inelastic deformation as the exposure temperature increases. This behavior is particularly evident in BCJ600 and BCJ800, for which the cumulative energy dissipation decreases by 46.47% and 75.64%, respectively, relative to BCJ20. Overall, the results demonstrate that elevated-temperature exposure substantially compromises the hysteretic energy dissipation capacity of the investigated beam–column joints. The reduction becomes increasingly pronounced as the temperature rises, with BCJ800 exhibiting the lowest cumulative energy dissipation and the smallest individual-loop energy measures. These findings highlight the importance of considering energy dissipation characteristics, in addition to strength and stiffness degradation, when evaluating the seismic performance of beam–column joints subjected to elevated temperatures. Figure 13 compares ductility degradation with the residual cumulative energy-dissipation capacity. The two indicators do not deteriorate at the same rate: at 800 °C, ductility decreases by approximately 40.8%, whereas cumulative energy dissipation decreases by 75.6%. This difference indicates that a joint may retain some displacement-based deformation capacity while losing a much larger share of its ability to dissipate energy over repeated cycles. Energy-based measures therefore provide complementary information to ductility and peak-load measures in the post-fire assessment of the modeled joints.

Table 7. Hysteretic energy dissipation parameters of the beam–column joint models at different temperatures

Model	Cumulative dissipated energy (J)	Largest loop area (J)	Average loop area (J)	Reduction in cumulative energy vs BCJ-L20 (%)
BCJ-L20	53,969.50	6,350.68	2,075.75	0
BCJ-L200	44,093.08	5,188.51	1,695.89	18.30
BCJ-L600	28,889.79	3,399.51	1,111.15	46.47
BCJ-L800	13,144.85	1,546.78	505.57	75.64

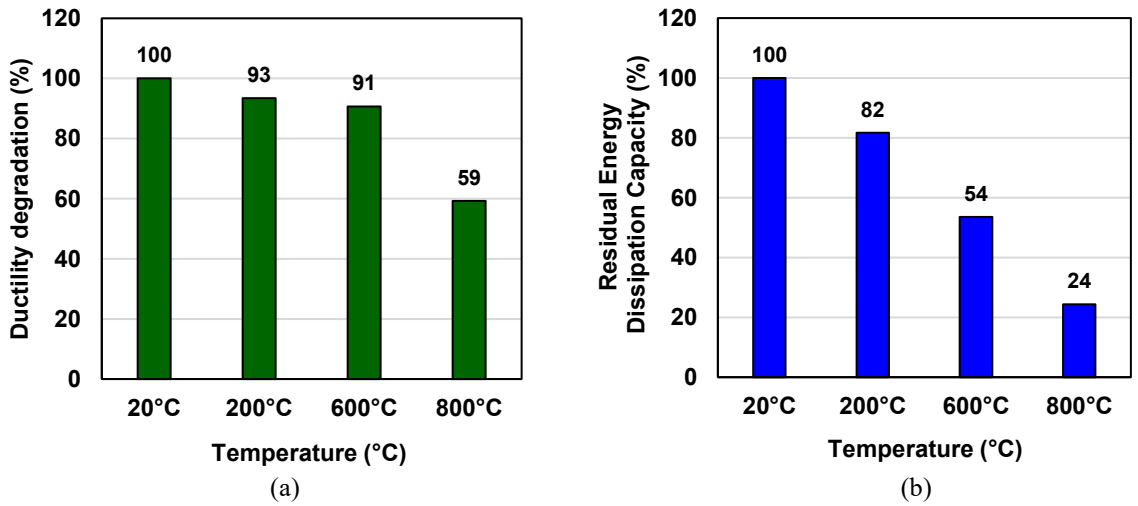


Figure 13. Degradation of seismic performance indicators for the LWAC beam-column joint models at different exposure temperatures: (a) Ductility degradation (%); (b) Residual energy dissipation capacity (%).

6. Conclusions

This study used sequential thermal and mechanical finite-element analyses to examine the cyclic response of LWAC beam–column joints after exposure to 200, 600, and 800 °C. Within the assumptions and limitations of the model, the principal findings are as follows:

1. Peak load decreased with increasing exposure temperature. The maximum loads were approximately 117 kN for BCJ-L20 and 101, 74, and 48 kN for BCJ-L200, BCJ-L600, and BCJ-L800, respectively. These values correspond to reductions of about 14%, 37%, and 59% relative to the ambient-temperature model.
2. The displacement at which the backbone response began to degrade decreased from 11.7 mm for BCJ-L20 to 10.6, 9.9, and 3.9 mm for BCJ-L200, BCJ-L600, and BCJ-L800, respectively. The strongest reduction occurred at 800 °C, indicating a substantially earlier loss of resistance in the most severely heated model.
3. Yield load decreased from 103 kN in BCJ-L20 to 91.4, 69.4, and 39.6 kN at 200, 600, and 800 °C, respectively. The corresponding yield displacements were 12.6, 12.8, 11.6, and 9.94 mm, while ultimate displacement decreased from 49.8 mm to 47.2, 41.7, and 23.3 mm.
4. Displacement ductility decreased from 3.95 for BCJ-L20 to 3.69, 3.58, and 2.34 for BCJ-L200, BCJ-L600, and BCJ-L800, representing reductions of approximately 6.6%, 9.4%, and 40.8%. The marked decline at 800 °C highlights the loss of deformation capacity under severe thermal exposure.
5. Cumulative hysteretic energy dissipation decreased from 53,969.50 J for BCJ-L20 to 44,093.08 J, 28,889.79 J, and 13,144.85 J for the models exposed to 200, 600, and 800 °C. The corresponding reductions were 18.30%, 46.47%, and 75.64%, respectively. Energy dissipation was more sensitive to temperature than displacement ductility, particularly at 600 and 800 °C.

The study is limited by the absence of direct experimental validation for the specific LWAC joint configuration, the use of averaged temperature-dependent properties from the literature, the simplified bond-slip representation, and the exclusion of the post-fire cooling stage. Validation against published normal-aggregate concrete joint tests supports the general modeling approach but does not remove these limitations. Future work should include experiments on LWAC beam–column joints subjected to heating and subsequent cyclic loading, improved characterization of bond-slip and spalling, and evaluation of cooling-history effects.

References

1. Ahmad, N., et al., *Nonlinear Modeling of RC Substandard Beam–Column Joints for Building Response Analysis in Support of Seismic Risk Assessment and Loss Estimation.* Buildings, 2022. **12**(10): p. 1758.
2. Bao, Y. and K.H. Tan, *Performance of precast concrete beam-column joint with a hidden corbel under progressive collapse scenarios.* Engineering Structures, 2022. **267**: p. 114679.
3. Angiolilli, M., et al., *Structural performance of unreinforced full-scale façade concrete beam-column joint under cyclic load.* Procedia Structural Integrity, 2023. **44**: p. 870–877.
4. Al-Rousan, R., et al., *Cyclic behavior of FRP strengthened beam-column joints under various concrete damage levels.* Construction Materials, 2023. **3**(1): p. 38–61.

5. Qin, D., et al., *A comprehensive review on fire damage assessment of reinforced concrete structures.* Case Studies in Construction Materials, 2022. **16**: p. e00843.
6. Biradar, G., N. Ramanna, and S.R.C. Madduru, *An in-depth examination of fire-related damages in reinforced concrete structures-A review.* Journal of Building Pathology and Rehabilitation, 2024. **9**(1): p. 81.
7. Noor, U.A., M.F. Javed, and K. Shahzada, *Experimental and numerical approaches for evaluating steel fiber reinforced concrete beam column joints: A state-of-the-art review.* Advances in Structural Engineering, 2025: p. 13694332251344651.
8. Pires, V., et al., *Evaluating building stones: Physical-mechanical changes from high-temperature fire and water cooling.* Heliyon, 2024. **10**(16).
9. Esmaeili, K., *An Introduction to Lightweight Flexible Nonlinear Composite (LFNLC) and Elastic Composite, Reinforced Lightweight Concrete (ECRLC) as the Cementitious LFNLC: Lightweight Flexible Nonlinear Composite.* International Journal of Innovation in Engineering, 2023. **3**(3): p. 28–47.
10. Othuman Mydin, M.A., *Evaluation of the mechanical properties of lightweight foamed concrete at varying elevated temperatures.* Fire, 2023. **6**(2): p. 53.
11. Jassim, W., M. Madhat, and A. Ali, *The Uses of Lightweight Material in Civil Engineering: A Review.* Al-Rafidain Journal of Engineering Sciences, 2024: p. 300–318.
12. Behera, D., et al., *Innovations and Applications in Lightweight Concrete: Review of Current Practices and Future Directions.* Buildings, 2025. **15**(12): p. 2113.
13. Zhang, F., et al., *Impact of High-Water-Absorption Recycled Foamed Basalt on Lightweight Aggregate Concrete Performance.* Iranian Journal of Science and Technology, Transactions of Civil Engineering, 2025: p. 1–18.
14. Chung, S.-Y., et al., *Development and microstructural characterization of ultra-lightweight aggregate concrete incorporating different sizes of polypropylene fibers.* International Journal of Concrete Structures and Materials, 2024. **18**(1): p. 86.
15. Lin, G., et al., *Balancing mechanical strength and thermal insulation in basalt fiber-reinforced ceramsite concrete (BFRCC): Microscopic mechanism analysis and multi-objective optimization.* Construction and Building Materials, 2025. **491**: p. 142660.
16. Bošnjak, J., A. Das, and A. Sharma, *Influence of concrete cover and transverse reinforcement on residual post-fire bond performance of reinforcement in concrete.* Engineering Structures, 2024. **314**: p. 118191.
17. Wang, Y., et al., *Bond-behavior of PCM-fire damaged concrete interface under hygrothermal environment.* Construction and Building Materials, 2024. **455**: p. 139171.
18. Kodur, V. and A. Gil, *Fire hazard in concrete bridges: review, assessment and mitigation strategies.* Structure and Infrastructure Engineering, 2024. **20**(10): p. 1577–1594.
19. Zhang, Y., et al., *Fire and post-fire performance of unbonded semi-precast prestressed reinforced concrete beams.* Engineering Structures, 2024. **308**: p. 117961.
20. Anand, V. and I.C. Christov, *On the enhancement of heat transfer and reduction of entropy generation by asymmetric slip in pressure-driven non-Newtonian microflows.* Journal of Heat Transfer, 2019. **141**(2): p. 022403.
21. Dashti, S., B.O. Caglayan, and N. Dashti, *Post-Earthquake Fire Resistance in Structures: A Review of Current Research and Future Directions.* Applied Sciences, 2025. **15**(6): p. 3311.
22. Ghobarah, A. and A. Said, *Shear strengthening of beam-column joints.* Engineering structures, 2002. **24**(7): p. 881–888.
23. Masi, A., G. Santarsiero, and D. Nigro, *Cyclic tests on external RC beam-column joints: role of seismic design level and axial load value on the ultimate capacity.* Journal of Earthquake Engineering, 2013. **17**(1): p. 110–136.
24. Rodrigues, H., et al., *Damage evolution in reinforced concrete columns subjected to biaxial loading.* Bulletin of earthquake Engineering, 2013. **11**(5): p. 1517–1540.
25. Melo, J., H. Varum, and T. Rossetto, *Experimental cyclic behaviour of RC columns with plain bars and proposal for Eurocode 8 formula improvement.* Engineering Structures, 2015. **88**: p. 22–36.
26. Izadifard, R. and A. Hajishabanian, *Experimental study on the post-fire seismic behavior of exterior beam-column joints in reinforced concrete frames.* Case Studies in Construction Materials, 2024. **21**: p. e03939.
27. Wu, Z., et al., *Post-earthquake fire resistance of self-centering concrete beam-column joint: An experimental investigation.* Engineering Structures, 2024. **305**: p. 117689.
28. Naeem, M.A., S. Shaikot, and M. Rashid, *PERFORMANCE OF BEAM COLUMN JOINT EXPOSED TO ELEVATED TEMPERATURE.*
29. Abdullah, A.H. and S.D. Mohammed, *Effect of lightweight expanded clay aggregate as partial replacement of coarse aggregate on the mechanical properties of fire-exposed concrete.* Journal of the Mechanical Behavior of Materials, 2023. **32**(1): p. 20220299.
30. Felicetti, R., P.G. Gambarova, and P. Bamonte, *Thermal and mechanical properties of light-weight concrete exposed to high temperature.* Fire and Materials, 2013. **37**(3): p. 200–216.

31. Chen, F., et al., *Study on the bond-slip numerical simulation in the analysis of reinforced concrete wall-beam-slab joint under cyclic loading.* Construction and Building Materials, 2024. **449**: p. 138266.
32. Pothisiri, T. and P. Panedpojaman, *Modeling of bonding between steel rebar and concrete at elevated temperatures.* Construction and Building Materials, 2012. **27**(1): p. 130–140.
33. Etemadi, E. and K. Fallahnezhad, *Behavior of reinforced concrete interior wide beam-column connections under lateral loading: A finite element study.* International journal of engineering and technology, 2017. **9**(3): p. 2559–2570.
34. Mofid, T. and H. Tavakoli, *Experimental Investigation of Cyclic Degradation of Light RC Beams under Periodic Loading.* Journal of Structural and Construction Engineering, 2021. **8**(Special Issue 2): p. 243–263.
35. Mofid, T. and H. Tavakoli. *Experimental investigation of mechanical behavior of lightweight RC elements under repeated loadings*. in *Structures*. 2023. Elsevier.
36. Tavakoli, H.R., T. Mofid, and M. Dehestani, *Dynamic analysis of thermal crack propagation in RCD dams considering rotational component of ground motion.* 2023.
37. Mofid, T. and H. Tavakoli, *Experimental investigation of post-earthquake behavior of RC beams.* Journal of Building Engineering, 2020. **32**: p. 101673.
38. En, C., 1-1, Eurocode 4: Design of composite steel and concrete structures. 1994, Part.
39. Européen, C., Eurocode 2: Design of concrete structures—Part 1-1: General rules and rules for buildings. London: British Standard Institution, 2004: p. 37.
40. Fu, F., *Advanced modelling techniques in structural design*. 2015: John Wiley & Sons.
41. Fu, F., *3D finite element analysis of the whole-building behavior of tall building in fire.* Advances in Computational Design, 2016. **1**(4): p. 329–344.
42. Fu, F., *Design and analysis of tall and complex structures*. 2018: Butterworth-Heinemann.
43. Fu, F., *Fire induced progressive collapse potential assessment of steel framed buildings using machine learning.* Journal of Constructional Steel Research, 2020. **166**: p. 105918.
44. Abu, A., et al., *Steel and Composite Structures*, in *International Handbook of Structural Fire Engineering*. 2021, Springer. p. 189–233.
45. Massumi, A., et al., *Development and Implementation of Staged Numerical Approaches for Post-Fire Seismic Assessment of Rc Beam-Column Joints.* Available at SSRN 5292775.
46. Bao, J., et al., *Thermal resistance, water absorption and microstructure of high-strength self-compacting lightweight aggregate concrete (HSSC-LWAC) after exposure to elevated temperatures.* Construction and Building Materials, 2023. **365**: p. 130071.
47. Guo, Z., et al., *The development of a component-based model for extended endplate joints in fire-induced progressive collapse scenarios.* Journal of Constructional Steel Research, 2025. **225**: p. 109182.
48. Abadel, A.A., *Physical, mechanical, and microstructure characteristics of ultra-high-performance concrete containing lightweight aggregates.* Materials, 2023. **16**(13): p. 4883.
49. Alhamad, A., et al., *Performance of different concrete types exposed to elevated temperatures: a review.* Materials, 2022. **15**(14): p. 5032.
50. Ataabadi, H.S., et al., *Lightweight dense polymer concrete exposed to chemical condition and various temperatures: An experimental investigation.* Journal of Building Engineering, 2021. **34**: p. 101878.
51. Bahrami, A. and M. Nematzadeh, *Effect of rock wool waste on compressive behavior of pumice lightweight aggregate concrete after elevated temperature exposure.* Fire Technology, 2021. **57**(3): p. 1425–1456.
52. Bao, J., et al., *A state-of-the-art review on high temperature resistance of lightweight aggregate high-strength concrete.* Journal of Building Engineering, 2023. **69**: p. 106267.
53. Chung, S.-Y., et al., *Effect of different expanded aggregates on durability-related characteristics of lightweight aggregate concrete.* Materials Characterization, 2021. **173**: p. 110907.
54. Dabbaghi, F., M. Dehestani, and H. Yousefpour, *Residual mechanical properties of concrete containing lightweight expanded clay aggregate (LECA) after exposure to elevated temperatures.* Structural Concrete, 2022. **23**(4): p. 2162–2184.
55. Dabbaghi, F., et al., *Evaluation of fracture energy, toughness, brittleness, and fracture process zone properties for lightweight concrete exposed to high temperatures.* Theoretical and Applied Fracture Mechanics, 2021. **116**: p. 103088.
56. Dabbaghi, F., et al., *Investigation on optimal lightweight expanded clay aggregate concrete at high temperature based on deep neural network.* Structural Concrete, 2022. **23**(6): p. 3727–3753.
57. Dabbaghi, F., et al., *Experimental and numerical investigation on post-fire seismic performance of light weight aggregate reinforced concrete beams.* Engineering Structures, 2022. **268**: p. 114791.
58. Dener, M., M. Karatas, and M. Mohabbi, *High temperature resistance of self compacting alkali activated slag/portland cement composite using lightweight aggregate.* Construction and Building Materials, 2021. **290**: p. 123250.

59. Hlavička, V., L.E. Hlavicka-Laczak, and E. Lubloy, *Residual fracture mechanical properties of quartz and expanded clay aggregate concrete subjected to elevated temperature.* Construction and Building Materials, 2022. **328**: p. 126845.
60. Humur, G. and A. Cevik, *Mechanical characterization of lightweight engineered geopolymer composites exposed to elevated temperatures.* Ceramics International, 2022. **48**(10): p. 13634–13650.
61. Lee, T., K. Jeong, and H. Choi, *Effect of thermal properties of aggregates on the mechanical properties of high strength concrete under loading and high temperature conditions.* Materials, 2021. **14**(20): p. 6093.
62. Martínez-Martínez, J.E., et al., *Assessment of lightweight concrete thermal properties at elevated temperatures.* Applied Sciences, 2021. **11**(21): p. 10023.
63. Meftah, H. and N. Arabi, *Effects of elevated temperatures' exposure on the properties of concrete incorporating recycled concrete aggregates.* Construction and Building Materials, 2024. **411**: p. 134612.
64. Nemes, R., et al., *Behavior of structural lightweight concrete produced with expanded clay aggregate and after exposure to high temperatures.* Journal of Thermal Analysis and Calorimetry, 2022. **147**(15): p. 8111–8118.
65. Pettmann, M., et al., *A comprehensive study of damage mechanisms in very lightweight aggregates concretes submitted to high temperatures.* Construction and Building Materials, 2023. **404**: p. 133251.
66. Pongsopha, P., et al., *Sustainable rubberized concrete mixed with surface treated PCM lightweight aggregates subjected to high temperature cycle.* Construction and Building Materials, 2021. **303**: p. 124535.
67. Roufael, G., et al., *Influence of lightweight aggregates on the physical and mechanical residual properties of concrete subjected to high temperatures.* Construction and Building Materials, 2021. **268**: p. 121221.
68. Sarıdemir, M. and S. Çelikten, *Effect of high temperature, acid and sulfate on properties of alkali-activated lightweight aggregate concretes.* Construction and Building Materials, 2022. **317**: p. 125886.
69. Shafigh, P., et al., *Influence of different ambient temperatures on the thermal properties of fiber-reinforced structural lightweight aggregate concrete.* Buildings, 2022. **12**(6): p. 771.
70. Tanhadoust, A., et al., *Predicting stress-strain behavior of normal weight and lightweight aggregate concrete exposed to high temperature using LSTM recurrent neural network.* Construction and Building Materials, 2023. **362**: p. 129703.
71. Tayeh, B.A., et al., *Effect of elevated temperatures on mechanical properties of lightweight geopolymer concrete.* Case Studies in Construction Materials, 2021. **15**: p. e00673.
72. Turkey, F.A., et al., *Effect of high temperatures on the properties of lightweight geopolymer concrete based fly ash and glass powder mixtures.* Case Studies in Construction Materials, 2022. **17**: p. e01489.
73. Li, S., et al., *General prediction models for local bearing capacity of concrete.* KSCE Journal of Civil Engineering, 2023. **27**(11): p. 4865–4875.
74. Sidoroff, F. *Description of anisotropic damage application to elasticity*. in *Physical non-linearities in structural analysis: symposium senlis, France May 27–30, 1980*. 1981. Springer.
75. Shen, R., L. Feng, and K. Rong, *Evaluation of rebar mechanical properties after high temperature (Fire Exposure).* Sichuan Building Science, 1991. **2**: p. 5–9.
76. Shi, K., et al., *Analysis on the seismic performance of steel fiber-reinforced high-strength concrete beam–column joints.* Materials, 2021. **14**(14): p. 4016.
77. Kenari, M.A., G. Abdollahzadeh, and S.K. Hashemi, *Experimental and numerical post-fire seismic performance assessment of recycled aggregate concrete beam-column joints.* Construction and Building Materials, 2025. **505**: p. 144617.

Supplementary Files

This is a list of supplementary files associated with this preprint. Click to download.

- HighLights.docx